Electronic structure of BaSnO$_3$ investigated by high-energy-resolution electron energy-loss spectroscopy and ab initio calculations

Hwanhui Yun, Mehmet Topsakal, Abhinav Prakash, Koustav Ganguly, Chris Leighton, Bharat Jalan, Renata M. Wentzcovitch, K. Andre Mkhoyan, and Jong Seok Jeong

---

Articles you may be interested in

Mobility-electron density relation probed via controlled oxygen vacancy doping in epitaxial BaSnO$_3$
APL Materials **5**, 056102 (2017); 10.1063/1.4983039

Room temperature spin Kondo effect and intermixing in Co/Cu non-local spin valves
Applied Physics Letters **110**, 222407 (2017); 10.1063/1.4984896

Adsorption-controlled growth of La-doped BaSnO$_3$ by molecular-beam epitaxy
APL Materials **5**, 116107 (2017); 10.1063/1.5001839

Structure and transport in high pressure oxygen sputter-deposited BaSnO$_{3-\delta}$
APL Materials **3**, 062509 (2015); 10.1063/1.4919969

Hybrid molecular beam epitaxy for the growth of stoichiometric BaSnO$_3$
Journal of Vacuum Science & Technology A: Vacuum, Surfaces, and Films **33**, 060608 (2015); 10.1116/1.4933401

Atomic and electronic structure of exfoliated black phosorus
Journal of Vacuum Science & Technology A: Vacuum, Surfaces, and Films **33**, 060604 (2015); 10.1116/1.4926753

Electronic structure of BaSnO₃ investigated by high-energy-resolution electron energy-loss spectroscopy and *ab initio* calculations

Hwanhui Yun, Mehmet Topsakal, Abhinav Prakash, Koustav Ganguly, Chris Leighton, Bharat Jalan, Renata M. Wentzcovitch, K. Andre Mkhoyan,[a] and Jong Seok Jeong[b]

Department of Chemical Engineering and Materials Science, University of Minnesota, Minneapolis, Minnesota 55455

There has been growing interest in perovskite $BaSnO_3$ due to its desirable properties for oxide electronic devices, including high electron mobility at room temperature and optical transparency. As these electronic and optical properties originate largely from the electronic structure of the material, here the basic electronic structure of epitaxially grown $BaSnO_3$ films is studied using high-energy-resolution electron energy-loss spectroscopy in a transmission electron microscope and *ab initio* calculations. This study provides a detailed description of the dielectric function of $BaSnO_3$, including the energies of bulk plasmon excitations and critical interband electronic transitions, the band structure and partial densities of states, the measured band gap, and more. *Published by the AVS.* https://doi.org/10.1116/1.5026298

I. INTRODUCTION

Perovskite structure $BaSnO_3$ has gained increasing attention recently as a candidate material for next-generation oxide electronic devices. This material has shown notably high electron mobility at room temperature, reported to be up to $320\,cm^2\,V^{-1}\,s^{-1}$ in bulk single crystal[1,2] and up to $183\,cm^2\,V^{-1}\,s^{-1}$ in epitaxial thin films of La-doped $BaSnO_3$,[3,4] with good optical transparency in the visible region. These properties are desirable in transparent conducting materials for solar cells, displays, high-mobility channels for transistors, and other applications.[5–9] Recent successes in thin film growth of epitaxial $BaSnO_3$ using vacuum deposition techniques[3,4,10–12] have opened up new possibilities to engineer various heterostructures based on this material and to improve its electron mobility through defect control, polarization doping, etc.[7,9,13,14] However, to optimize the potential use of this material, it is essential to measure and understand the electronic structure of $BaSnO_3$ in order to elucidate the mechanisms for high carrier mobility. To this end, there have been several previous *ab initio* studies and optical measurements to understand various properties of $BaSnO_3$. Electronic band structures have been calculated,[15–18] and the conduction band edge effective mass,[19] band gap energy,[9,20,21] and dielectric constant[22] have been experimentally determined.

One of the ways to study the electronic properties of a material is through a combination of *ab initio* calculations of its band structure, from which all electronic properties can be deduced, and experimental electron energy-loss spectroscopy (EELS). EELS provides an experimental confirmation of the accuracy of calculated band structure, which can be achieved by: (1) comparison between measured and calculated density of states (DOS) uniquely defined by the band structure and (2) comparison between the measured and calculated interband electronic transitions from valence to conduction bands, also uniquely defined by band structure. Once such agreements are established, electronic properties of the material deduced from the band structure confirmed can be used with confidence.

Here, we report comprehensive information on the electronic structure of $BaSnO_3$ using high-energy-resolution EELS in a scanning transmission electron microscope (STEM). We have acquired high-energy-resolution EELS spectra at elemental edges and compared them with *ab initio* predictions to examine the electronic structure of $BaSnO_3$. The low-loss region (0–50 eV) of EELS has been used to study the dielectric properties, including interband electronic transitions and plasmon excitations. In the high-loss region (>50 eV), the fine structure of core-edges reveals the details of the conduction band by directly probing the element-specific empty DOS of the material. Good agreement between experimentally measured EELS spectra and the results of *ab initio* calculations provides critical reliability for the details of the electronic structure of $BaSnO_3$ reported here.

II. METHODS

A. Sample preparation

An epitaxial, single-phase $BaSnO_3$ film was grown on a $SrTiO_3(001)$ substrate by hybrid molecular beam epitaxy,[10] targeting the film thickness of 72 nm. Cross-sectional transmission electron microscopy samples were prepared by using a focused ion beam (FEI Quanta 200 3D) lift out method, where the samples were thinned by a 30 kV Ga-ion beam and then cleaned with a 5 kV Ga-ion beam. The samples were further polished by Ar-ion milling using a Fischione 1010 ion mill and a Gatan precision ion polishing system. This sample preparation provides us with relatively damage-free and electron-transparent samples. Many samples and areas were used in these measurements. The thicknesses of the samples were estimated from low-loss EELS data using the EELS log-ratio method,[23] and they were in the range of 20–40 nm. The mean free path of plasmon

---

a)Electronic mail: mkhoyan@umn.edu
b)Electronic mail: jsjeong@umn.edu

excitation was calculated to be 81 nm (Ref. 23) for the BaSnO$_3$ under our experimental conditions.

B. STEM imaging and EELS data acquisition

STEM imaging and EELS measurements were carried out using an aberration-corrected FEI Titan G2 60-300 (S)TEM equipped with a CEOS DCOR probe corrector, a Schottky extreme field emission gun, a monochromator, and a Gatan Enfinium ER spectrometer. The microscope was operated at 200 keV. The semiconvergence angle of the STEM probe was 15 mrad, and the beam current was set to 50 pA. High-angle annular dark-field (HAADF) images were recorded with a detector angle of 42–200 mrad, and the collection angle of the EELS was 29 mrad. A dual EELS mode, which simultaneously collects the low-loss region including a zero-loss peak (ZLP) and high-loss region, was used to correct the energy alignment, when needed. Energy dispersions of 0.05 and 0.1 eV per channel were used to measure low-loss and core-loss data, while EELS data for detailed analysis of interband electronic transitions were acquired with an energy dispersion of 0.01 eV per channel. Energy resolutions for these dispersion values, estimated from the full-width at half maximum (FWHM) of the ZLPs, were 0.4, 0.25, and 0.13 eV for 0.1, 0.05, and 0.01 eV per channel, respectively. For an accurate determination of peak positions, the alignment and dispersion values of the spectrometer were calibrated using reference peaks of Si $L_{2,3}$ of SiO$_2$ (108.3 eV), π* of graphite (285.37 eV), and Ni L_3 of NiO (852.75 eV).[23] All EELS spectra were obtained from the central regions of BaSnO$_3$ films in order to minimize the influence of the film-substrate interface and surface. In our early studies, we found that the critical thickness of BaSnO$_3$ films is less than 2.5 nm on SrTiO$_3$(001).[24] Therefore, all the EELS results presented here are from fully relaxed films. EELS acquisition was performed in the beam spot mode. By simply assuming the beam size and the sample thickness to be 0.1 and 40 nm, interactive volume was estimated to be about 16 nm^3 for each acquisition in the spot mode. To increase the signal-to-noise ratio, two-three spectra from adjacent regions were acquired and averaged.

C. *Ab initio* calculations

Ab initio calculations were performed using the WIEN2K code.[25–27] A generalized gradient approximation (GGA) using Perdew–Burke–Ernzenhof (PBE) parametrization[28] was adopted for the electronic exchange and correlation functional. The Brillouin zone was sampled at a $16 \times 16 \times 16$ shifted k-point grid using the tetrahedron method.[29] The wave functions were expanded in spherical harmonics inside nonoverlapping atomic spheres of radius R_{MT} (muffin-tin radii) and in plane waves for the remaining space of the unit cell. R_{MT} values for Ba, Sn, and O were set at WIEN2K defaults: 2.50 a.u. for Ba, 2.11 a.u. for Sn, and 1.82 a.u. for O. The plane wave expansion in the interstitial region was determined by a cutoff wave vector chosen to be $k_{max} = 7.0/R_{MT}$. Empty states up to 4.0 Ry ($= 54.4$ eV) above the Fermi level, E$_F$, were included in the calculations. To ensure reliability of our calculations, we also performed band structure calculations using Heyd–Scuseria–Ernzerhof (HSE06)[30] and modified Becke–Johnson (mBJ)[31] parametrizations for comparison, and they all produced very similar band structures for BaSnO$_3$ (not presented here), despite differences in the band gap values (2.52 eV for HSE06 and 2.37 eV for mBJ). Frequency dependent dielectric matrix calculations within the independent particle random phase approximation were performed using the OPTIC module of WIEN2K, as detailed in Ref. 32. O K edge EELS simulations were performed using the TELNES3 module of WIEN2K with calculation parameters from the experimental setup. Core-hole effects were included by using a $2 \times 2 \times 2$ supercell containing 40 atoms (8 Ba, 8 Sn, and 24 O), and a core–hole was incorporated into an absorbing oxygen atom. Because calculations using GGA with PBE parameterization are known to result in a smaller band gap than experimental results,[16,18] the band gap, which is 0.41 eV from PBE, was adjusted to the measured value of 3.0 eV by a simple scissor operation. Calculations for band structure, DOS, and dielectric function include spin–orbit (SO) interactions.

III. RESULTS AND DISCUSSION

Figure 1 shows HAADF-STEM images of the BaSnO$_3$ film that were used for EELS analysis in this work. From the
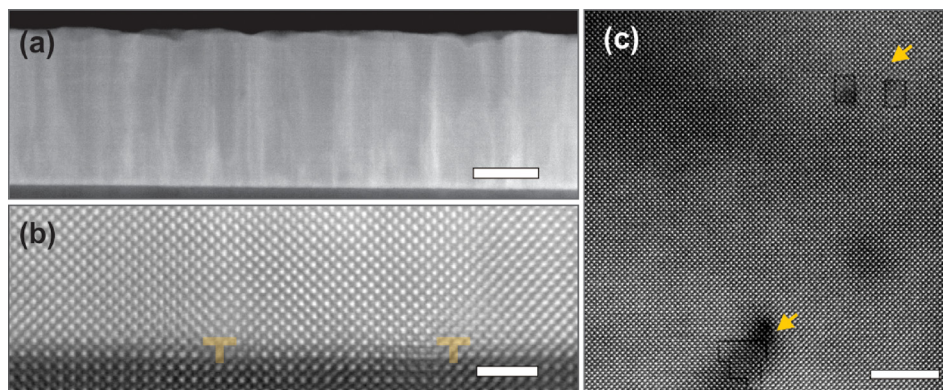
FIG. 1. (Color online) (a) Low- and (b) high-magnification cross-sectional HAADF-STEM images of 72 nm-thick BaSnO$_3$ film on a SrTiO$_3$(001) substrate. Atomic-resolution HAADF-STEM images at the interface is shown in (b). The image is filtered using "HRTEM Filter" in GATAN DIGITALMICROGRAPH software (Refs. 34 and 35). The filtering parameters are described in Ref. 36. Misfit dislocations at the interface are marked with dislocation symbols. (c) plan-view HAADF-STEM images of the BaSnO$_3$ film. Ruddlesden–Popper faults are indicated by arrows. Scale bar is 30, 2, and 5 nm in (a)–(c), respectively.

FIG. 2. Calculated real, ε_1, and imaginary, ε_2, parts of the dielectric function of BaSnO₃. The bulk plasmon energies (I, E_P) in ε_1 and direct interband transition peaks (a to k) in ε_2 are marked.

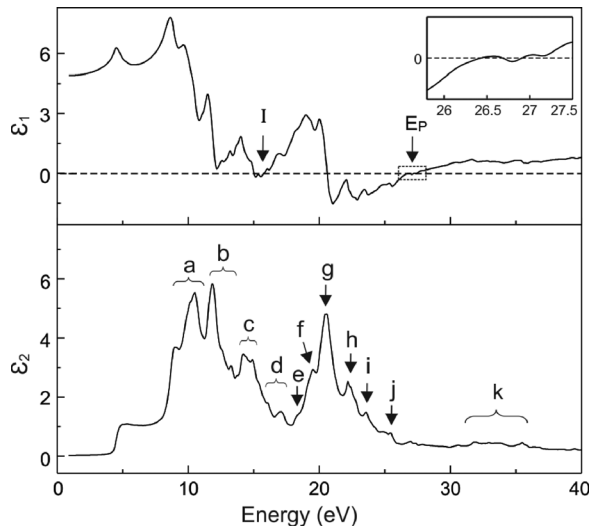cross-sectional HAADF-STEM images, the film thickness was measured to be 72 nm. High-resolution HAADF-STEM images demonstrate that these BaSnO₃ films are indeed epitaxially grown on the substrate and form a sharp interface with a relatively low surface roughness. Misfit dislocations are observed as expected. Figure 1(c) shows a plan-view HAADF-STEM image displaying epitaxially grown BaSnO₃ crystal without any voids or amorphous regions. Previously reported Ruddlesden–Popper faults are also monitored.[33]

A. Calculated dielectric function and band structure

The calculated dielectric function of BaSnO₃ is shown in Fig. 2. The complex dielectric function $\varepsilon(E) = \varepsilon_1(E) + i\varepsilon_2(E)$ describes how the electron gas in materials responds to an applied electromagnetic field.[23,37–42] The energy where the real part of the dielectric function, $\varepsilon_1(E)$, changes from

negative to positive, evidences a bulk plasmon due to collective oscillations of the electrons. The calculated $\varepsilon_1(E)$ indicates that bulk plasmon excitations can be expected at 15.2, 26.4, and 26.9 eV in BaSnO₃, as marked as I and E_P in Fig. 2. The inset figure shows the very close two plasmon energies of 26.4 and 26.9 eV. In the imaginary part of the dielectric function, $\varepsilon_2(E)$, peaks correspond to the direct interband electronic transitions.[23,37–42] Distinguishable peaks in $\varepsilon_2(E)$ are marked with arrows and labeled in Fig. 2, and details are discussed in Sec. III C.

The calculated band structure and DOS of BaSnO₃ are shown in Fig. 3. The results are essentially consistent with previous reports.[17,18,20,43,44] The conduction band minimum is positioned at the Γ point (0, 0, 0) and the valence band maximum is at the R point (0.5, 0.5, 0.5) in reciprocal space. The curvatures at these points also predict an effective mass of the electrons in conduction band, $m_e^* = 0.54m_0$, and effective mass of the holes in valence band, $m_h^* = -10.7m_0$, which are important parameters determining charge carrier mobilities. Figure 3(b) shows that the lower conduction bands from 3 to 8 eV consist predominantly of s and p states of Sn and O, and the conduction bands above 8 eV are mainly composed of d and f states of Ba. The O $2p$ states are dominant in the upper valence band, and high-density Ba $5p$ states are found at around −10 eV. The principal quantum number resolved partial density of states (pDOS) of Ba, Sn, and O are shown in Fig. 3(b). The pDOS data were used to identify possible interband electronic transitions in $\varepsilon_2(E)$ and $Im[-1/\varepsilon]$, and the low-loss EELS spectra in Sec. III C.

B. Band gap measurement

The band gap of BaSnO₃ films was measured using high-energy-resolution low-loss EELS data. To measure the band gap from the low-loss EELS data, the ZLP was removed as follows: (1) a tail of zero-loss EELS spectrum was acquired in vacuum, (2) it was fitted to the low-loss EELS spectra in the 1–2.5 eV range using a multiple linear regression
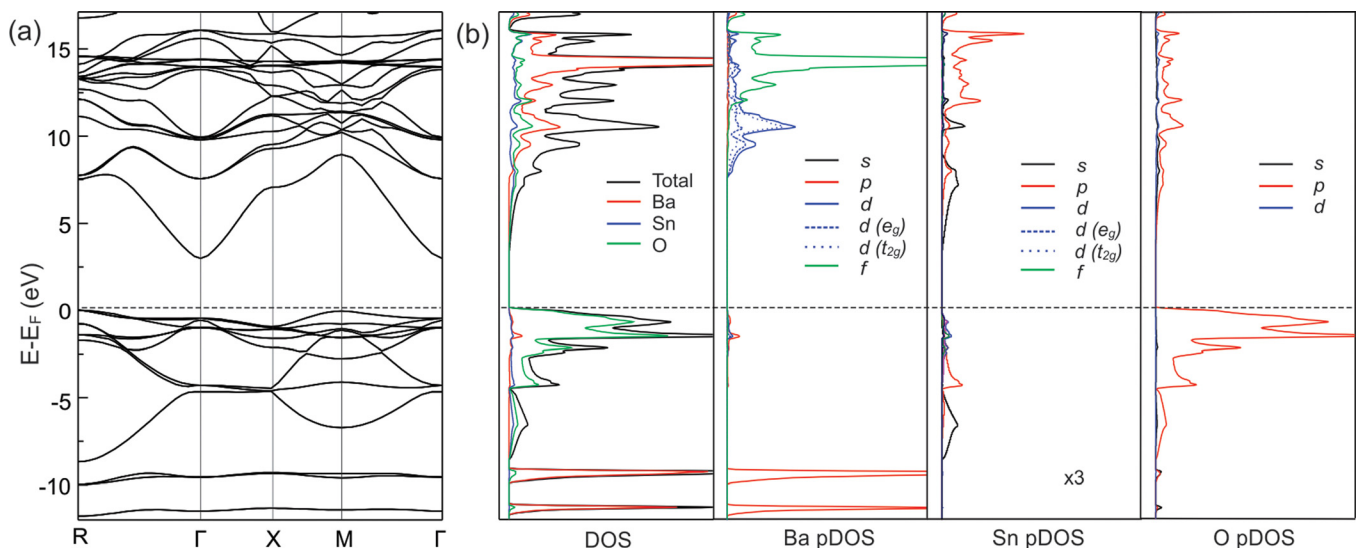

FIG. 3. (Color online) Calculated band structure (a) and corresponding DOS (b) of BaSnO₃: total DOS and elementally resolved pDOS of Ba, Sn, and O. Here, E_F is at the valence band maximum.
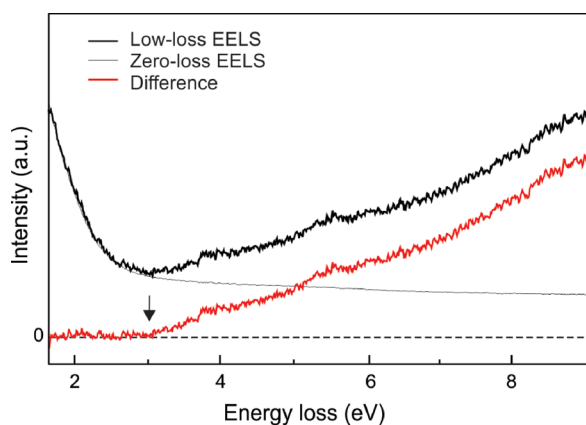
FIG. 4. (Color online) High-energy-resolution low-loss EELS spectrum obtained from a BaSnO₃ film. The zero-loss EELS, obtained in vacuum, was fitted to the low-loss EELS spectrum and then subtracted from the spectrum to get the difference. The onset of the difference, which corresponds to the band gap, is indicated by an arrow.

method, and (3) the fitted tail of the zero-loss EELS spectrum was subtracted from the low-loss EELS data.[45] To improve statistics, 22 spectra from the BaSnO₃ film were analyzed. One representative example is shown in Fig. 4. The onset value of the ZLP-subtracted spectrum indicates the band gap energy. The measured band gap energy for the BaSnO₃ film was 3.0 ± 0.1 eV. To confirm the validity of this method, the same analysis was applied to the SrTiO₃ substrate and the resulting band gap energy was 3.3 ± 0.1 eV, which is consistent with well documented SrTiO₃ band gap energy of 3.25 eV.[46] The band gap energy of BaSnO₃ films from our measurements are compared with the values reported in the literature in Table I. A band gap energy of 3.0 eV is used for all subsequent analyses.

C. Low-loss EELS analysis

Low-loss EELS spectra were measured on the BaSnO₃ film and compared with the electron energy-loss function calculated from the dielectric function. The energy-loss spectrum of incident probe electrons, which travel through a sample and act as an electromagnetic wave, can be deduced from the imaginary part of the inverse dielectric function, as it is proportional to $Im[-1/\varepsilon]$ [or $\varepsilon_2/(\varepsilon_1^2 + \varepsilon_2^2)$].[23,37–42] To account for the energy spread of the incident electron beam, the calculated $Im[-1/\varepsilon]$ was convolved with a Gaussian function.[50] The FWHM of the Gaussian function was set to

TABLE I. Experimentally measured band gap energy (E_g) of BaSnO₃ from the literature.

E_g (eV)			
Direct	Indirect	Method	References
	3.0 ± 0.1	Low-loss EELS	This work
3.56 ± 0.05	2.93 ± 0.05	Ellipsometry	9
3.12	2.85	Diffuse reflectance	47
3.1	2.95	Transmittance	48
3.4		Reflectance	49

be the FWHM of the ZLP for each data set. The measured low-loss EELS spectra from BaSnO₃ films and the calculated $Im[-1/\varepsilon]$ are then compared, as can be seen in Fig. 5. For more quantitative analysis, the peak positions are compared in Table II. The overall shape and peak positions from the calculation and the experimental measurements are in good agreement. However, there are noticeable differences between the calculated $Im[-1/\varepsilon]$ and the measured low-loss EELS spectra because: (1) the calculation underestimates damping of plasmon oscillations[23,37] and (2) the contributions from surface plasmons and Cerenkov radiation are not included in the calculations.[51,52] It should be noted that while core-loss Sn $N_{4,5}$ and Ba $O_{2,3}$ edges are included in the calculation, the peaks due to these electronic transitions should be interpreted with caution; the Sn $4d^{3/2}$ and $4d^{5/2}$ and Ba $5p^{1/2}$ and $5p^{3/2}$ core-levels in these calculations are treated as "semicore" levels without the core-hole effects. The effects of SO interactions on these edges can be seen in comparison between two calculated $Im[-1/\varepsilon]$, shown in Fig. 5(b).
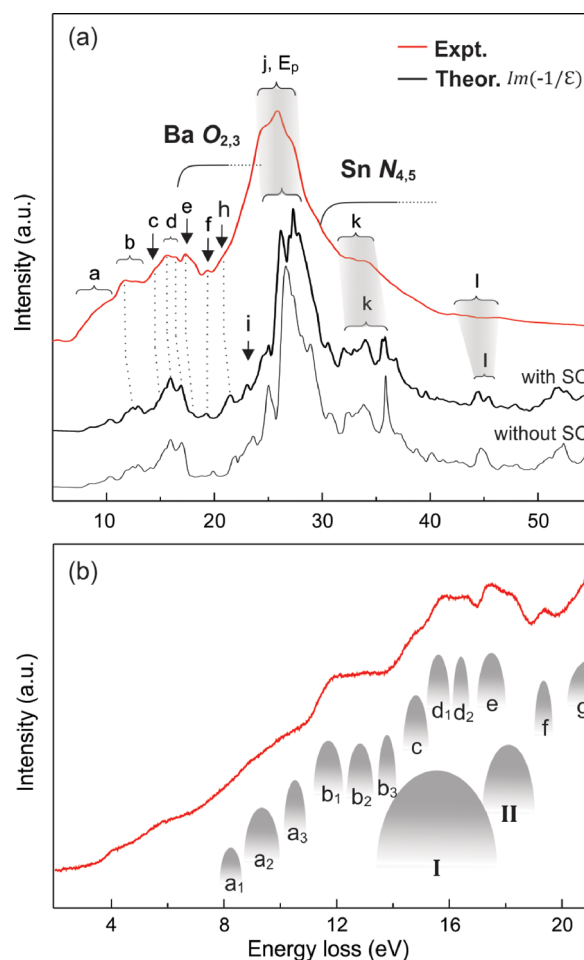
FIG. 5. (Color online) (a) Comparison of experimental low-loss EELS spectrum from the BaSnO₃ film and calculated $Im[-1/\varepsilon]$. The peaks from interband electronic transitions are labeled from a to l. The bulk plasmon peak, E_P, and the Sn $N_{4,5}$ and Ba $O_{2,3}$ edges are also indicated. For comparison, calculated $Im[-1/\varepsilon]$ without SO interactions is also plotted as well. (b) High-energy-resolution low-loss EELS spectra from the same BaSnO₃ film. Possible interband transitions, predicted from theory, are indicated with the labels. The peaks I and II represent predicted second bulk and surface plasmon peak, respectively.

Tᴀʙʟᴇ II. Peak positions (in eV) from plasmon excitations and interband electronic transitions. The peaks are labeled as in Figs. 2 and 5 and compared to the predicted transitions from the calculated ε, $Im[-1/\varepsilon]$, and pDOS with assignments. Transitions from initial Sn $4d$ and Ba $5p$ states are not considered here.

Group	Peaks	Experiment	Theory				Assignment
Plasmon	E_P	25–27	26.4, 26.9				First bulk plasmon
	I	—	15.2				Second bulk plasmon
	II	—	18.7, 19.0				Surface plasmon
			From ε_2	From $Im[-1/\varepsilon]$	From pDOS	Initial state	Final state
Interband	a_1	—	8.3	8.4	7.8, 8.5	O $2p$	Sn $5s$
	a_2	—	9.5, 9.8	9.6	9.3, 10.1	O $2p$	Sn $5s$
	a_3	—	10.4	10.3	10.2, 10.9	O $2p$	Ba $5d$
	b_1	~12	11.2, 12.0	11.9, 12.4	11.4, 12.1, 12.7	O $2p$	Sn $5s$
					11.2, 11.7, 12.0	O $2p$	Ba $5d$
					11.4, 12.1	Sn $5p$	Sn $5s$
	b_2	~13	12.7	12.9	12.7	O $2p$	Sn $5s$
					12.8	O $2p$	Ba $5d$
	b_3	~14	13.6	13.7, 14.0	13.6	Ba $5d$	Ba $4f$
					13.7	O $2p$	Ba $5d$
					13.7	Sn $5p$	Ba $5d$
	c	~15	14.4	14.2	14.4	Ba $5d$	Ba $4f$
			14.8	~14.7	14.7	O $2p$	Sn $5s$
					14.8	O $2p$	Ba $5d$
					14.8	Sn $5p$	Ba $5d$
	d_1	15.8	15.6	15.9	15.6	Ba $5d$	Ba $4f$
	d_2	16.6	16.5	16.9	16.4	Ba $5d$	Ba $4f$
	e	17.5	~17.8	17.8	17.4	Ba $5d$	Sn $5p$
	f	19.4	19.1	19.2	19.4	Sn $5s$	Sn $5p$
	g	—	20.1		—	—	—
	h	~21	21.8, 22.0, 22.4	~21.5	—	—	—
	i	—	23.1	23.2	—	—	—
	j	24.7, 26.4, 27.3	26.1, 27.3	26.6, 27.0, 27.5	—	—	—
	k	32.7, 34.5	31.7, 32.8, 35.4	31.9, 34.0, 35.8,			
	l	42.5, 46.5	44.2, 45.2	44.5, 45.4	—	—	—

As was discussed earlier, the theoretical bulk plasmon energies are 26.4 and 26.9 eV. In low-loss EELS, the bulk plasmon peak is part of a broader peak [labeled as "j" in Fig. 5(a)], which includes peaks from fine structure of the Ba O$_{2,3}$ edge. The overall agreement between the experimentally observed plasmon energy of $E_P = 25–27$ eV and theoretical prediction is quite good. It should be noted that plasmon damping induces broadening and a slight shift of plasmon peaks; the plasmon linewidth, ΔE_P, which is the FWHM of a plasmon peak, is determined by the plasmon damping constant, and the plasmon peak position shifts slightly from E_P to a lower value of $\sqrt{E_P^2 - (\Delta E_P^2/2)}$.[23] Because phonons and defects are not considered in the calculations, plasmon damping through these mechanisms are not included.[53,54] As a result, better match between the theoretical and the experimental bulk plasmon peaks should not be expected.[55] An additional plasmon peak at 15.2 eV is also predicted from the calculated dielectric function, as discussed earlier. We speculate that this plasmon represents oscillations of electrons in a subsidiary band near the valence band, but this needs further study. Due to several peaks from interband transitions and surface plasmons, this plasmon peak is not clearly identifiable in the low-loss EELS data. As

stated earlier, the experimental low-loss EELS includes other contributions, such as surface plasmon peaks, in contrast to the calculation. The surface plasmon peak is expected to be at around 18.8 eV from $E_{SP} = E_P/\sqrt{2}$;[23,37,38,42] however, such a peak is not discernible as it is superimposed on strong interband transition peaks.

The peaks, labeled from a to l in low-loss EELS in Fig. 5(a), result from interband electronic transitions (see Fig. 2). More detailed fine structure of these peaks is shown in Fig. 5(b), where the peaks from a, b, and d are further resolved and labeled using subscripts. The second bulk and surface plasmon peaks (I and II), which were discussed earlier, are also presented. To interpret the interband transition peaks, the energy levels with high-density electronic states were examined from a calculated pDOS [see Fig. 3(b)] and the possible interband electronic transitions from valence band to conduction band were investigated within the selection rules.[56] For easy comparison, the peaks predicted from the possible interband transitions are indicated as labeled from a to g in Fig. 5(b). The energies of the majority of these interband electronic transition are identified from experimental low-loss EELS spectra as well as from calculated imaginary part of the dielectric function and from peaks of $Im[-1/\varepsilon]$. The results are tabulated, and
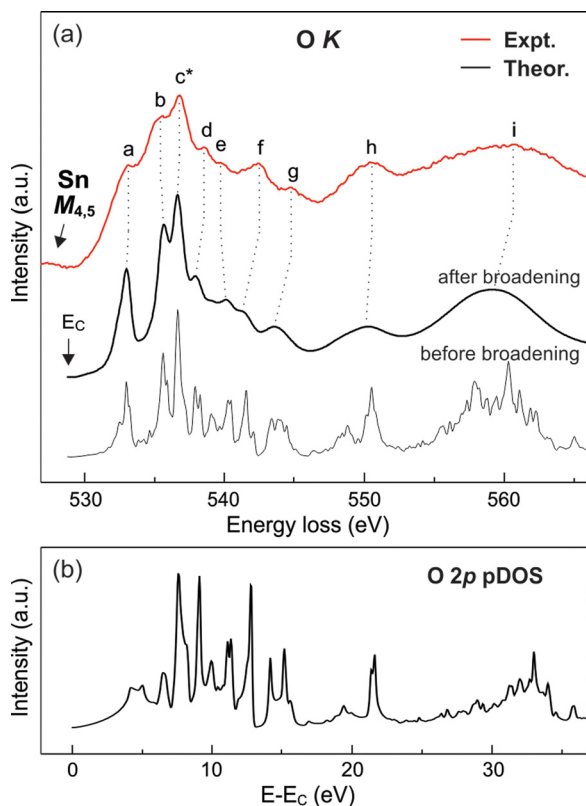
FIG. 6. (Color online) (a) Comparison of experimental EELS O K edge from the BaSnO$_3$ film and simulated O K edge. The peak c* was used as a reference for the alignment. The simulated O K edge EELS includes effects of core-hole and angular integration covering experimental probe convergence and EELS collection angles; before (thin line) and after (thick line) implementing energy broadening. The onset of the EELS O K edge representing the minimum of the conduction band, E_C, is indicated using an arrow. The identifiable peaks are labeled and compared in Table III. Note that the O K edge overlaps with the tail of the Sn $M_{4,5}$ edge. (b) The calculated ground state O $2p$ pDOS of the conduction band in BaSnO$_3$ that was used to calculate the spectrum in (a).

the assigned interband electronic transitions are summarized in Table II.

D. Core-loss EELS analysis

High-energy-resolution O K edge EELS spectra were measured from the BaSnO$_3$ film and compared with the O K edge simulation result generated using the WIEN2K code including the core-hole effects. A double differential cross section for core-level electronic transitions is calculated from the calculated ground state O $2p$ pDOS modified by the core-hole effects; $\partial^2\sigma/\partial E\partial\Omega \propto \sum_{i,f} |M_{i,f}|^2 \text{DOS}(E)$, where Ω is the scattering solid angle and $M_{i,f}$ is the transition matrix element.[57,58] This double differential cross section is then integrated using experimental STEM probe convergence and EELS collection angles.[25,59] The results are presented in Fig. 6 as the theoretical EELS before broadening. The effects of core-hole are quite substantial while the effects of angular integration covering experimental probe convergence and EELS collection angles are minor due to their wide range relative to Brillouin zone of BaSnO$_3$. An energy spreading of the incident electron beam was implemented by

convolving the simulation result with a Gaussian function with the FWHM of the ZLP. Next, the natural energy broadening, which arises from the lifetime of the electrons in the initial and final states of excitation, was taken into account.[23,60,61] The energy level width of the initial O $1s$ state, Γ_i, is as small as 0.153 eV. In contrast, the energy level width of the final state, Γ_f, is considerable and varies with energy relative to the conduction band minimum (or onset energy of core-loss edge). The Γ_f for O $2p$ increases from 0 to 6 eV with increasing the energy from 0 to 40 eV above the onset energy.[60] The energy broadening due to the lifetime effect (for both initial and final states) can be represented by a Lorentzian function.[50] Thus, the simulated O K edge was further convolved with Lorentzian functions with the FWHM of the Γ_i and Γ_f, consecutively, to implement the natural energy broadening. The resulting O K edge is compared to the experimental O K edge EELS spectrum obtained from the BaSnO$_3$ film in Fig. 6 as the theoretical EELS after broadening. The match is good, further proving reliability of this analysis. The remaining discrepancies can be attributed to the fact that the O K edge sits on the tail of the Sn $M_{4,5}$ edge and defects present in the actual samples are not accounted for in the calculations. The peak positions from the experimental O K edge EELS spectrum and the simulation result are summarized in Table III. This comparison also allows the determination of the buried onset of the EELS O K edge, which represents the minimum of the conduction band, E_C, at 528.9 eV.

The Sn $M_{4,5}$ edge and Ba $N_{4,5}$ and $M_{4,5}$ edges were also measured. The results are shown in Fig. 7. The Ba $N_{4,5}$ edge has a delayed maximum with detectable fine structure generated by the excitation of Ba $4d$ electrons [Fig. 7(a)]. The Sn $M_{4,5}$ edge, which is attributed to the excitation of Sn $3d$ electrons, is mostly positioned just before the O K edge, as shown in Fig. 7(b). The overall peak shape follows a delayed maximum shape and is similar to that from SnO$_2$,[62] indicating the presence of Sn in the 4+ oxidation state. Due to a high density of unfilled Ba $4f$ orbitals above the Fermi energy, the Ba $M_{4,5}$ edge appears as two strong white lines: M_5 (labeled as n) and M_4 (labeled as o), separated by 15 eV. In a simple single-electron excitation description, the two peaks are explained via SO splitting.[63] The $3d^{5/2}$ (M_5) and $3d^{3/2}$ (M_4) initial states are split due to the SO interaction,

TABLE III. Comparison of peak positions from the experimental and the simulated O K edge EELS shown in Fig. 6. The peak c* is used for alignment.

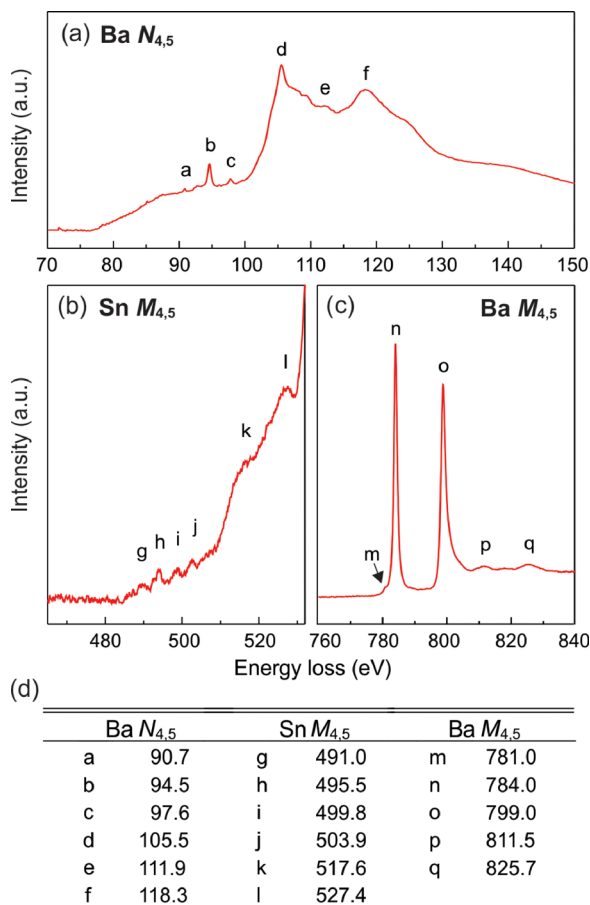|	Expt. (eV)	Theor. (eV)
a	533.3	533.2
b	535.5	535.8
c*	536.8	536.8
d	538.6	538.2
e	539.9	540.4
f	542.5	541.5
g	545.0	543.8
h	550.7	550.5
i	560.6	559.4

FIG. 7. (Color online) Measured core-loss EELS spectra from the BaSnO$_3$ film: (a) Ba $N_{4,5}$ edge, (b) Sn $M_{4,5}$ edge, and (c) Ba $M_{4,5}$ edge. (d) List of experimental peak positions of Ba $N_{4,5}$, Ba $M_{4,5}$, and Sn $M_{4,5}$ EELS edges fine structure shown in panels (a)–(c).

with a 6:4 ratio of degeneracy of the states.[23,56] However, the ratio of integral intensity of M_5 and M_4 in experimental EELS was observed to be 0.83. The value deviates considerably from the 1.5 of the 6:4 ratio of degeneracy. Also, an additional prepeak (labeled as m) is observed ahead of the M_5 peak. It appears that this discrepancy is primarily due to the insufficient treatment of the overlap between the wave function of the $3d$ core–holes and the wave function of excited electrons which is not adequately treated in the simple single-electron excitation interpretation.[56] Using multiplet theory several reports showed that such a multielectron excitation effect can be incorporated into calculation when the electron–electron interaction, H_{ee}, and the SO interaction, H_{so}, are added into the Hamiltonian of the single-electron atomic model, H_{1s}, i.e., $H = H_{1s} + H_{ee} + H_{so}$.[56,63] When the H_{so} is negligible compared to the H_{ee}, the electronic states of an atom can be described using the LS coupling scheme, in which electronic states are determined by a given atomic configuration. By employing the LS coupling scheme, the initial and final electronic states and the available electronic transitions can be taken into consideration. Radtke and Botton,[63] using this approach, predicted three transitions for the excitations of Ba $4d$ electrons to Ba $4f$ orbitals, which effectively describe the observations of the

peaks, m, n, and o in the Ba $M_{4,5}$ edge as well as the low value of the M_5/M_4 ratio.[63]

IV. CONCLUSION

The electronic structure of the epitaxial BaSnO$_3$ film grown on SrTiO$_3$(001) was investigated using high-energy-resolution EELS in STEM and *ab initio* calculations. The indirect band gap energy was measured from the low-loss EELS to be 3.0 ± 0.1 eV. Experimental low-loss EELS spectrum, which is directly proportional to the electron energy-loss function, was compared with the calculated $Im[-1/\varepsilon]$ function and the observed peaks due to plasmon excitations and interband transitions were analyzed. The experimental bulk plasmon peak was observed at 25–27 eV while the theoretical value was predicted to be at 26.4 and 26.9 eV. The expected small discrepancy between the experimental and calculated bulk plasmon energy was explained through plasmon damping, which was not properly taken into account in "phonon-free" and "defect-free" *ab initio* calculations. The interband electronic transition peaks were clearly observed and their positions were identified in low-loss EELS. The results were compared with predictions based on the calculated pDOS, where the observed peaks were assigned to distinct interband transitions from the valence band to the conduction band.

The core-level electron excitations were also examined using the core-loss EELS edges. O K, Ba $N_{4,5}$, Sn $M_{4,5}$, and Ba $M_{4,5}$ edges were measured using high-energy-resolution EELS and their fine structures were analyzed. For comparison, a simpler O K edge, resulting from the excitation of O $1s$ electrons to the empty DOS above the Fermi energy, was simulated from calculated O $2p$ pDOS. When the instrumental and the natural energy broadenings were implemented into this simulation, the resulting theoretical O K edge was in very good agreement with the experimental O K edges, further confirming reliability of this analysis. The number of peaks and their relative intensities in Ba $M_{4,5}$ edge fine structure, which deviate from a simple SO interaction model with a 6:4 ratio of degeneracy, were explained by more rigorous atomic multiplet theory. Importantly, this work can be used as a starting point to explore the local electronic structure changes in BaSnO$_3$ films by structural defects, including dislocations, vacancies, interfaces, and impurity doping.

[1]X. Luo, Y. S. Oh, A. Sirenko, P. Gao, T. A. Tyson, K. Char, and S.-W. Cheong, Appl. Phys. Lett. **100**, 172112 (2012).
[2]H. J. Kim *et al.*, Appl. Phys. Express **5**, 061102 (2012).
[3]S. Raghavan, T. Schumann, H. Kim, J. Y. Zhang, T. A. Cain, and S. Stemmer, APL Mater. **4**, 016106 (2016).
[4]H. Paik *et al.*, APL Mater. **5**, 116107 (2017).
[5]H. M. Kim, U. Kim, C. Park, H. Kwon, and K. Char, APL Mater. **4**, 056105 (2016).
[6]U. Kim *et al.*, APL Mater. **3**, 036101 (2015).
[7]S. Ismail-Beigi, F. J. Walker, S. W. Cheong, K. M. Rabe, and C. H. Ahn, APL Mater. **3**, 062510 (2015).
[8]L. Zhu, Z. Shao, J. Ye, X. Zhang, X. Pan, and S. Dai, Chem. Commun. **52**, 970 (2016).
[9]S. A. Chambers, T. C. Kaspar, A. Prakash, G. Haugstad, and B. Jalan, Appl. Phys. Lett. **108**, 152104 (2016).
[10]A. Prakash, J. Dewey, H. Yun, J. S. Jeong, K. A. Mkhoyan, and B. Jalan, J. Vac. Sci. Technol., A **33**, 060608 (2015).
[11]Z. Lebens-Higgins *et al.*, Phys. Rev. Lett. **116**, 027602 (2016).
[12]U. S. Alaan, P. Shafer, A. T. Diaye, E. Arenholz, and Y. Suzuki, Appl. Phys. Lett. **108**, 042106 (2016).
[13]J. Shiogai, K. Nishihara, K. Sato, and A. Tsukazaki, AIP Adv. **6**, 065305 (2016).
[14]S. Yu, D. Yoon, and J. Son, Appl. Phys. Lett. **108**, 262101 (2016).
[15]H. Mizoguchi, H. W. Eng, and P. M. Woodward, Inorg. Chem. **43**, 1667 (2004).
[16]E. Moreira, J. M. Henriques, D. L. Azevedo, E. W. S. Caetano, V. N. Freire, U. L. Fulco, and E. L. Albuquerque, J. Appl. Phys. **112**, 043703 (2012).
[17]A. Slassi, Mater. Sci. Semicond. Process. **32**, 100 (2015).
[18]S. Soleimanpour and F. Kanjouri, Physica B **432**, 16 (2014).
[19]S. James Allen, S. Raghavan, T. Schumann, K. M. Law, and S. Stemmer, Appl. Phys. Lett. **108**, 252107 (2016).
[20]D. J. Singh, Q. Xu, and K. P. Ong, Appl. Phys. Lett. **104**, 011910 (2014).
[21]T. Schumann, S. Raghavan, K. Ahadi, H. Kim, and S. Stemmer, J. Vac. Sci. Technol., A **34**, 050601 (2016).
[22]P. Singh, B. J. Brandenburg, C. P. Sebastian, P. Singh, S. Singh, D. Kumar, and O. Parkash, Jpn. J. Appl. Phys. **47**, 3540 (2008).
[23]R. F. Egerton, *Electron Energy Loss Spectroscopy in the Electron Microscope* (Plenum, New York, 1996).
[24]K. Ganguly, P. Ambwani, P. Xu, J. S. Jeong, K. A. Mkhoyan, C. Leighton, and B. Jalan, APL Mater. **3**, 062509 (2015).
[25]P. Blaha, K. Schwarz, G. Madsen, D. Kvasnicka, and J. Luitz, *WIEN2k User's guide* (Vienna University of Technology, Vienna, Austria, 2014).
[26]K. Schwarz, P. Blaha, and G. K. H. Madsen, Comput. Phys. Commun. **147**, 71 (2002).
[27]K. Schwarz and P. Blaha, Comput. Mater. Sci. **28**, 259 (2003).
[28]J. P. Perdew, K. Burke, and M. Ernzerhof, Phys. Rev. Lett. **77**, 3865 (1996).
[29]P. E. Blöchl, O. Jepsen, and O. K. Andersen, Phys. Rev. B **49**, 16223 (1994).
[30]J. Heyd, G. E. Scuseria, and M. Ernzerhof, J. Chem. Phys. **118**, 8207 (1994).
[31]A. D. Becke and E. R. Johnson, J. Chem. Phys. **124**, 221101 (2006).
[32]C. Ambrosch-Draxl and J. O. Sofo, Comput. Phys. Commun. **175**, 1 (2006).
[33]W. Y. Wang, Y. L. Tang, T. L. Zhu, J. Suriyaprakash, Y. B. Xu, Y. Liu, B. Gao, S. W. Cheong, and X. L. Ma, Sci. Rep. **5**, 16097 (2015).
[34]D. Mitchell, "HRTEM Filter," Dave Mitchell's Digital Micrograph™ Scripting Website, accessed 5 November 2016, http://www.dmscripting.com/.
[35]R. Kilaas, J. Microsc. **190**, 45 (1998).
[36]The images were first filtered using a standard Wiener filter, which allows to remove the components of the image from amorphous parts of the specimen. Amorphous components of the images for an operation of a Wiener filter are estimated as follows: The Fast Fourier Transform (FFT) of an image is radially averaged and the averaged image is subtracted from the original FFT image iteratively to acquire signals from an amorphous region. Parameters of delta%, a step size, and the number of cycles are set for the procedure; Delta% is the upper limit of the % of pixels to be changed by each iteration, the step size determines the rate (and stability) of the convergence of iterations. Here, in our analysis, the Delta% was set to be 5%, the step size was 5, and the number of cycles used was 20. Then, the Butterworth filter was applied to remove high-frequency noise. The second order Butterworth filter was used with FWHM of 0.5.
[37]H. Raether, *Excitation of Plasmons and Interband Transitions by Electrons* (Springer-Verlag, Berlin, 1980).
[38]C. Kittel, *Introduction to Solid State Physics* (Wiley, New Jersey, 1996).
[39]G. Brockt and H. Lakner, Micron **31**, 435 (2000).
[40]P. Moreau and M. C. Cheynet, Ultramicroscopy **94**, 293 (2003).
[41]V. J. Keast, J. Electron. Spectrosc. Relat. Phenom. **143**, 97 (2005).
[42]Y. Sato, M. Terauchi, M. Mukai, T. Kaneyama, and K. Adachi, Ultramicroscopy **111**, 1381 (2011).
[43]B. G. Kim, J. Y. Jo, and S. W. Cheong, J. Solid State Chem. **197**, 134 (2013).
[44]Y. Li, L. Zhang, Y. Ma, and D. J. Singh, APL Mater. **3**, 011102 (2015).
[45]The tail of zero-loss EELS spectrum obtained from vacuum was fitted with the low-loss EELS spectra obtained from samples using multiple linear regression method with fitting function, $f_{fit}(E) = b + c * f_{ZL}(E)$, where $f_{fit}(E)$ is the fitting function to low-loss EELS data, $f_{ZL}(E)$ is the zero-loss spectrum obtained from vacuum, and b and c are coefficients. The energy window 1–2.5 eV used here for fitting contains more than 140 data points in each spectrum. R^2 values assessing the goodness-of-fit were in the range of 0.9855–0.9995 (average = 0.9961) for BaSnO₃ on LaAlO₃ samples and in the range of 0.9703 to 0.9985 (average 0.9939) for BaSnO₃ on SrTiO₃ samples.
[46]K. van Benthem, C. Elsässer, and R. H. French, J. Appl. Phys. **90**, 6156 (2001).
[47]B. Hadjarab, A. Bouguelia, and M. Trari, J. Phys. D: Appl. Phys. **40**, 5833 (2007).
[48]H. J. Kim *et al.*, Phys. Rev. B **86**, 165205 (2012).
[49]G. Larramona, C. Gutierrez, I. Pereira, M. R. Nunes, and F. M. A. da Costa, J. Chem. Soc. Faraday Trans. **85**, 907 (1989).
[50]G. K. Wertheim, M. A. Butler, K. W. West, and D. N. E. Buchanan, Rev. Sci. Instrum. **45**, 1369 (1974).
[51]J. Park, S. Heo, J. G. Chung, H. Kim, H. Lee, K. Kim, and G. S. Park, Ultramicroscopy **109**, 1183 (2009).
[52]L. Gu *et al.*, Phys. Rev. B **75**, 195214 (2007).
[53]F. Vaz, N. Martin, and M. Fenker, *Metallic Oxynitride Thin Films by Reactive Sputtering and Related Deposition Methods: Processes, Properties and Applications* (Bentham Science, Sharjah, 2013).
[54]A. Woessner *et al.*, Nat. Mater. **14**, 421 (2015).
[55]If accuracy is not critical, the bulk plasmon energy can also be estimated using a simple free electron model with the equation, $E_P = \hbar\sqrt{ne^2/m_e\epsilon_0}$, where n is the bulk density of valence electrons, e is the charge of an electron, m_e is the mass of an electron, and ϵ_0 is the vacuum permittivity. From this free electron model, the bulk plasmon energy of valence electrons in BaSnO₃ was calculated to be 26.0 eV, which is in reasonably good agreement with the experimental bulk plasmon energy. The n used for this calculation was 4.90×10^{29} m⁻³.
[56]F. de Groot and A. Kotani, *Core Level Spectroscopy of Solids* (CRC, Boca Raton, 2008).
[57]D. A. Muller, D. J. Singh, and J. Silcox, Phys. Rev. B **57**, 8181 (1998).
[58]K. A. Mkhoyan, J. Silcox, E. S. Alldredge, N. W. Ashcroft, H. Lu, W. J. Schaff, and L. F. Eastman, Appl. Phys. Lett. **82**, 1407 (2003).
[59]K. Jorissen, "The ab initio calculation of relativistic electron energy loss spectra," Ph.D. thesis (Univ. of Antwerp, 2007).
[60]R. F. Egerton, Micron **34**, 127 (2003).
[61]M. O. Krause, J. Phys. Chem. Ref. Data **8**, 307 (1979).
[62]M. S. Moreno, R. F. Egerton, and P. A. Midgley, Phys. Rev. B **69**, 233304 (2004).
[63]S. J. Pennycook and P. D. Nellist, *Scanning Transmission Electron Microscopy*, edited by S. J. Pennycook and P. D. Nellist (Springer, New York, 2011), pp. 207–246.